Lithuanian Journal of Physics
Vol. **66**, No. 3, pp. 154–163 (2026)
ISSN 1648-8504 eISSN 2424-3647
DOI: https://doi.org/10.3952/physics.2026.66.3.3

DANGLING BONDS IN HYDROXYLATED AND AMINATED NANODIAMONDS: APPLICATION OF THE GLOBAL OPTIMIZATION ALGORITHM

Š. Masys [a], V. Jonauskas [a], and Z. Rinkevicius [b]

[a] *Institute of Theoretical Physics and Astronomy, Faculty of Physics, Vilnius University, Saulėtekio 3, 10257 Vilnius, Lithuania*

[b] *Department of Theoretical Chemistry and Biology, School of Engineering Sciences in Chemistry, Biotechnology and Health, KTH Royal Institute of Technology, SE-10691 Stockholm, Sweden*

Email: sarunas.masys@tfai.vu.lt

Received 10 December 2025; revised 29 April 2026; accepted 30 April 2026

The geometric configuration of dangling bonds (DBs) – one of the most abundant paramagnetic defects in nanodiamonds (NDs) – is investigated by applying the global optimization algorithm (GOAT). A total of more than five million geometry optimization runs are carried out to search for the lowest-energy conformers of DBs introduced into hydroxylated and aminated NDs. An analysis of over 3,000 electronic *g*-tensor calculations performed for the obtained structures shows that only three unique DB types are present in octahedrally shaped $C_{35}(OH)_{36}$ and $C_{35}(NH_2)_{36}$ nanoparticles, enabling future studies on similar NDs with fully functionalized surfaces to consider a relatively small number of DBs and thereby save computational time and resources. It is also revealed that the arithmetically averaged isotropic *g*-shifts from the geometries of the standard optimization agree well with the GOAT results, although the behaviour of individual DBs is not properly captured.

Keywords: nanodiamonds, dangling bonds, geometry optimization, electronic *g*-tensor

1. Introduction

An impressive mixture of beneficial properties that nanodiamonds (NDs) possess [1] makes them attractive candidates in various fields of nanomedicine, including bioimaging, drug delivery, and bone tissue engineering [2]. Non-invasive bioimaging, for example, is crucial for improving pre-clinical diagnosis and therapy [3], as it allows the monitoring of drug distribution in the body, the tracking of treatment response, and the evaluation of drug delivery system effectiveness [4]. Although NDs can in principle be visualized by magnetic resonance imaging [5, 6] – a highly valued non-invasive modality, – the presence of paramagnetic impurities in NDs is an essential factor that enables the application of this technology. Given that dangling bonds (DBs) are among the most abundant paramagnetic defects in NDs [7], and hydroxylation as well as amination are among the most popular surface functionalizations exploited [8], DBs introduced into hydroxylated and aminated NDs have become the focus of our research.

In our previous work [9], NDs with hydroxylated and aminated surfaces were studied with respect to the magnetic properties, namely, the electronic *g*-tensor of their DBs. As one of the most important parameters of electron paramagnetic resonance (EPR), the *g*-tensor contains a wealth of information about the electronic and geometric structure of the investigated open-shell systems [10], while EPR itself is an invaluable tool to directly observe paramagnetic defects [11]. Needless to say, the *g*-tensor calculations were carried out after the geometry optimization of DBs [9]. However, due to the surface complexity of hydroxylated and aminated NDs, the standard optimization procedure does not necessarily guarantee the convergence to

their lowest-energy structures, which may affect the properties of interest. Luckily, the new release of the ORCA software [12] introduces the global optimization algorithm (GOAT) for molecules and atomic clusters [13]. In short, GOAT operates by performing cycles of uphill moves on the potential energy surface to cross energy barriers, followed by downhill optimizations to locate new minima. It uses a simulated annealing-like approach with a self-regulating fictitious temperature to determine the acceptance of new conformers. This tool finds global energy minima and relevant conformers without relying on molecular dynamics, making it computationally efficient and applicable to any regular quantum chemistry method. Combined with the ultrafast approximations such as GFN2-xTB [14], GOAT provides a solid platform for exploring the vast conformational space that the flexible surfaces of hydroxylated and aminated NDs possess. That being said, we decided to assess the reliability of our previous results [9] by employing the geometries of DBs obtained from the GOAT optimization. It should be emphasized that although the utilization of GOAT plays a central role in this study, our primary interest lies not in the geometries *per se*, but in how they affect the *g*-tensor values. On the one hand, a side-by-side comparison of distinct conformers is rather complicated, while on the other hand, the *g*-tensor is highly sensitive to the local environment and therefore perfectly reflects geometric differences. The GOAT optimization and subsequent *g*-tensor calculations were done for DBs introduced into octahedrally shaped $C_{35}(OH)_{36}$ and $C_{35}(NH_2)_{36}$ nanoparticles. An additional investigation also involved a slightly larger hydroxylated ND, $C_{51}(OH)_{52}$, of tetrahedral shape.

2. Computational details

All geometry optimizations were performed with the ultrafast semiempirical tight-binding GFN2-xTB method [14] via the xtb program package (version 6.7.1) [15] exploiting it as an external module for the ORCA quantum chemistry program suite (version 6.0.1) [12, 16, 17]. In order to mimic the water environment potentially important for the applications of NDs, the analytical linearized Poisson–Boltzmann solvation model [18] was used during those runs. Concerning the GOAT algorithm [13], the search for the global minimum was guided by the convergence of energy as well as the maximization of conformational entropy. For each GOAT step, the number of conducted geometry optimizations varied from 6,032 for $C_{35}(OH)_{36}$ to 9,288 for $C_{35}(NH_2)_{36}$ and 10,608 for $C_{51}(OH)_{52}$. Since between three and 11 GOAT steps were required for each considered DB, more than five million geometry optimization runs were carried out in total.

The electronic *g*-tensor calculations – more than 3,000 in total – were done using the thoroughly tested [19] combination of B3LYP/6-311G(2d,2p) [20–23] within the effective nuclear charge framework [24–26] that also incorporated the gauge-including atomic orbitals. In order to significantly reduce the computational time, the modified resolution of the identity [27] and chain of spheres [28] techniques were applied for the Coulomb and Hartree–Fock exchange interactions, respectively. def2/J [29] was chosen as an auxiliary Coulomb-fitting basis set. The isotropic *g*-shift values (or simply the isotropic *g*-shifts) $\Delta\bar{g}$ were computed by subtracting the free electron *g*-factor (g_e = 2.0023193) from the isotropic *g*-tensor values $\bar{g}$ and expressing the difference in parts per million (ppm). $\bar{g}$ was taken as an arithmetic average of the principal components g_{ii} ($i = x, y, z$) of the *g*-tensor which, in turn, was obtained as the positive square roots of the eigenvalues of $\mathbf{g}^T\cdot\mathbf{g}$.

In order to maintain the high level of precision, the convergence criteria for the single-point calculations as well as geometry relaxation procedures were tightened as it was done previously [9, 19 30–33]. Carbon DBs of a doublet electronic state were introduced into NDs by selectively removing OH or NH_2 groups, one at a time. All drawings presented in the study were produced with the visualization program VESTA [34].

3. Results and discussion

A visual representation of hydroxylated and aminated NDs is shown in Fig. 1. The results of the electronic *g*-tensor calculations for DBs introduced into $C_{35}(OH)_{36}$ and $C_{35}(NH_2)_{36}$ are provided in Figs. 2 and 3, respectively. In Fig. 2, one may observe that standard geometry optimization yields DB structures with a large variation in the isotropic *g*-shift values (red squares), which appear to be distributed in a quasi-uniform manner. The application of GOAT (blue

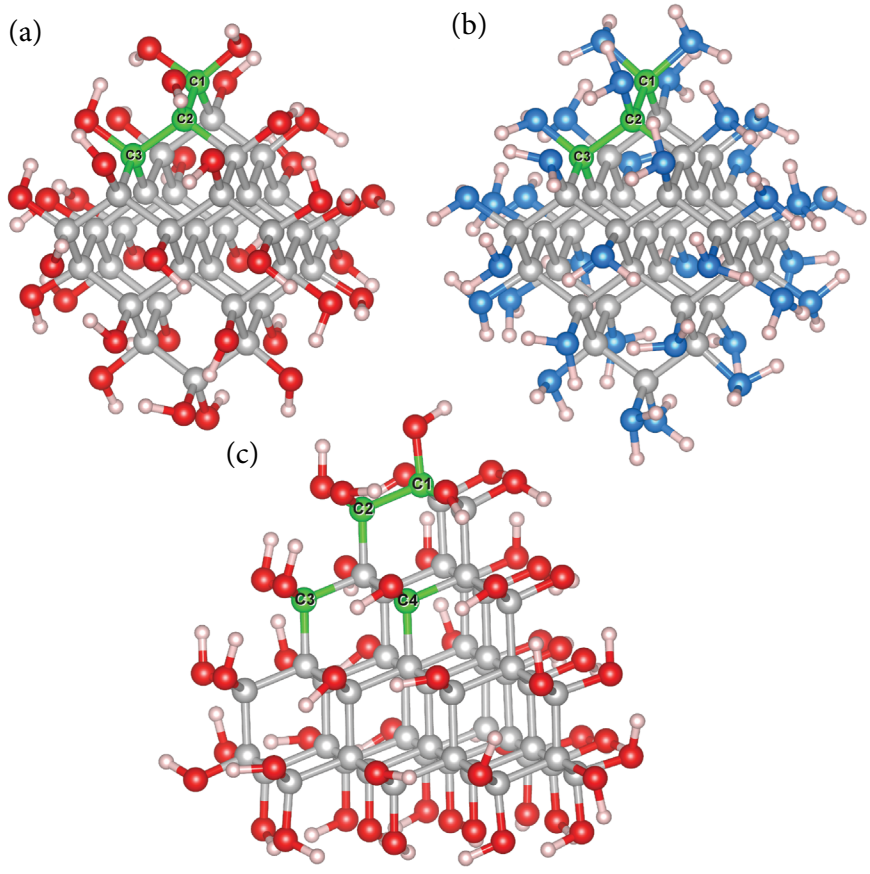

Fig. 1. Visualization of NDs: octahedral (a) $C_{35}(OH)_{36}$ and (b) $C_{35}(NH_2)_{36}$ as well as (c) tetrahedral $C_{51}(OH)_{52}$. Grey, red, azure and pink balls correspond to the carbon, oxygen, nitrogen and hydrogen atoms, respectively. Carbon atoms that represent the positions of unique DBs are labelled and for a better contrast marked in green.

circles), on the other hand, drastically changes the picture, as the lowest-energy structures found via this algorithm demonstrate three clearly separated regions of *g*-shifts. The first region comprises $\Delta\bar{g}$ values ranging from 221 to 267 ppm, the second from 464 to 559 ppm, and the third from 976 to 1005 ppm. However, the most important finding is that DBs belonging to the same region are of the same type. To be precise, DBs, the *g*-shift values of which fall in the first region, are of C2-type, as marked in Fig. 1(a), whereas the second region contains C3-type DBs and the third region consists of C1-type DBs. Generally speaking, $C_{35}(OH)_{36}$ is functionalized with 36 hydroxyl groups, and the removal of each will result in 36 individual DBs. For a system with a simpler surface functionalization, such as $C_{35}H_{36}$, it is easy to prove that only three of the 36 available DBs are unique by comparing their *g*-shifts after the standard geometry optimization [19] (a comparison of energies alone is not reliable since very similar energies can correspond to quite different geometries). Unfortunately, this is not the case concerning hydroxylated or aminated NDs due to their more complex surface composition. In our previous studies [9, 32] based on the standard geometry optimization, we raised an assumption that hydroxylated and aminated NDs might not possess geometrically equivalent DBs, but they do possess geometrically similar ones. The GOAT data given in Fig. 2 indicate that, rather than being merely geometrically similar, DBs in these systems appear to be geometrically equivalent. However, a rigorous proof of their equivalence – by demonstrating identical $\Delta\bar{g}$ values in the selected region – is complicated because of the vast conformational space that must be explored. Nevertheless, something can still be done to improve the situation. In order to fully exploit the conformational diversity unravelled by GOAT, we extended our analysis by performing *g*-tensor calculations

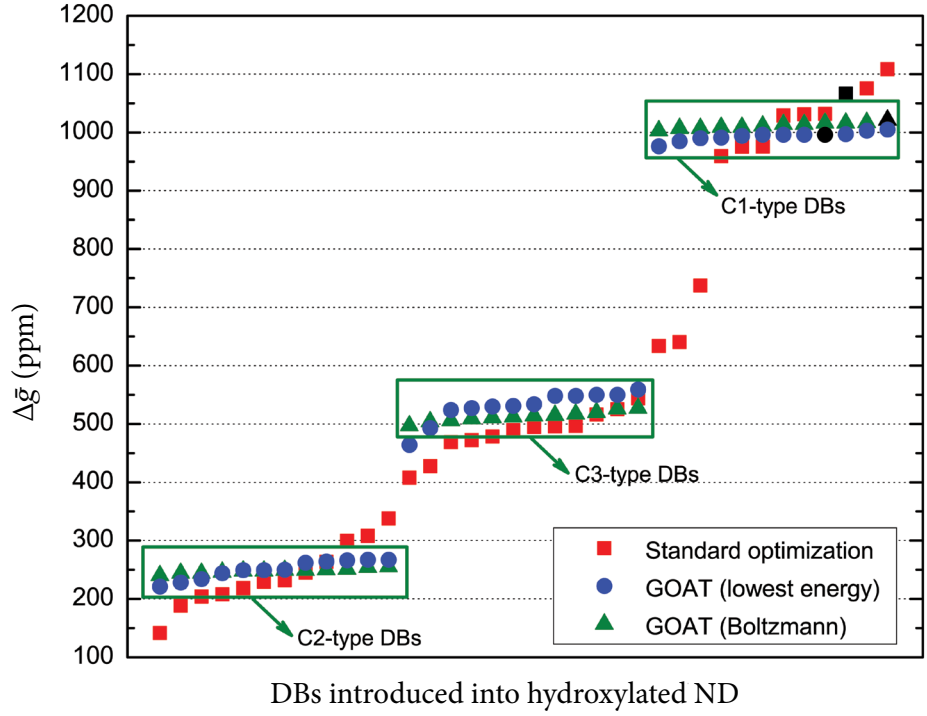

Fig. 2. Isotropic *g*-shifts $\Delta\tilde{g}$ calculated for all possible DB positions in $C_{35}(OH)_{36}$ after standard and GOAT optimizations. Black symbols represent DBs that possess the lowest energy among all considered DBs. For clarity, green boxes indicate GOAT (Boltzmann) data points associated with the same DB type.

for the 30 energetically lowest structures of each DB. The contribution of the considered conformers was evaluated by applying the Boltzmann distribution at a temperature of 300 K, meaning that every new GOAT data point (green triangles) actually represents the Boltzmann-weighted average of the isotropic *g*-shifts for the 30 lowest-energy conformers of a particular DB. On the one hand, such treatment provides a better approximation of real-world conditions, which naturally account for thermal effects, while on the other, it leads to a narrower distribution of the *g*-shift values. To be concrete, the variation range of $\Delta\tilde{g}$ decreases from 46 to 15 ppm for C2-type DBs (the first region), from 95 to 30 ppm for C3-type DBs (the second region), and from 29 to 18 ppm for C1-type DBs (the third region). Given that 30 ppm corresponds to the error margin of a high-precision EPR experiment, it is clear that the Boltzmann-weighted averages exhibit minimal deviations, which, in principle, confirms the idea that only three unique DB types comprising 12 geometrically equivalent DBs each exist in $C_{35}(OH)_{36}$. The physical origin of their uniqueness is determined by the local surface environment in ND: C1-type DBs are positioned at the vertices, while C2-type and C3-type DBs are located at the edges of ND. The distinction between C2-type and C3-type DBs is that the former ones are situated in the vicinity of the vertices, whereas the latter ones are not, with a non-OH-bonded carbon atom neighbouring them. One more thing to note regarding the analysis of data is that both the standard and GOAT optimizations identify the lowest-energy DBs (black symbols) as C1-type or irregular (i.e. formed of the OH-bonded dangling C atom).

The data for $C_{35}(NH_2)_{36}$, presented in Fig. 3, are rather different from what was seen in the case of hydroxylated ND. Although the *g*-shifts obtained after the standard geometry optimization (red squares) are also distributed in a quasi-uniform manner, the span of their values is much narrower now, reaching only 314 ppm (277 to 591 ppm) compared to 967 ppm (142 to 1109 ppm) for $C_{35}(OH)_{36}$. Such a narrow range naturally makes it more challenging to distinguish regions of the geometrically equivalent DBs. And indeed, an employment of GOAT with Boltzmann-weighted averaging for the 30 lowest-energy conformers of each DB (blue circles) results in one apparently separated region

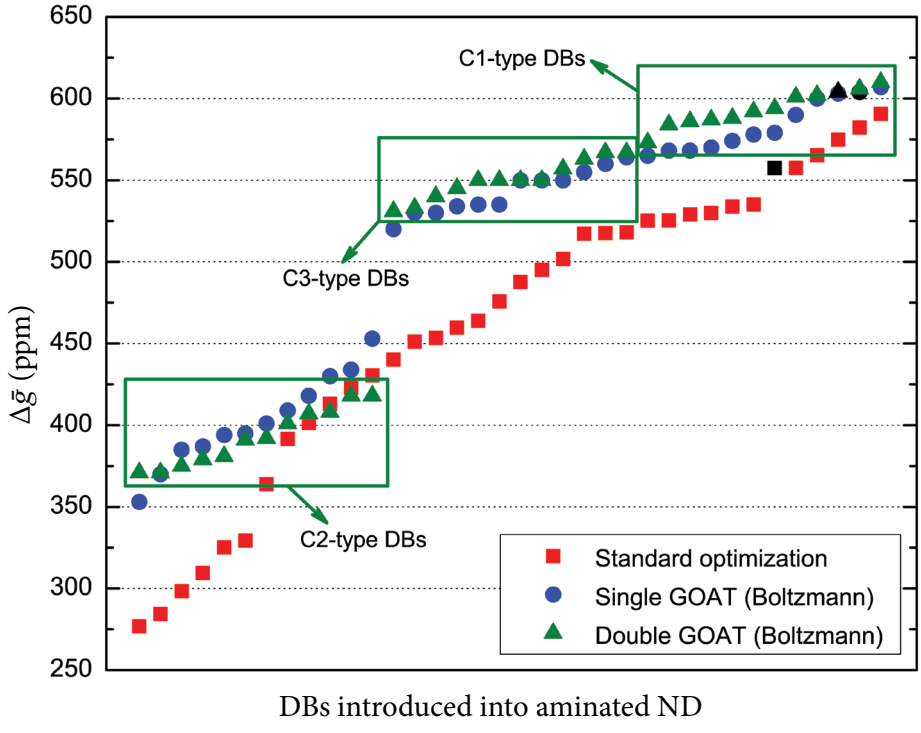

Fig. 3. Isotropic *g*-shifts $\Delta\bar{g}$ calculated for all possible DB positions in $C_{35}(NH_2)_{36}$ after standard and GOAT optimizations. Black symbols represent DBs that possess the lowest energy among all considered DBs. For clarity, green boxes indicate double GOAT (Boltzmann) data points associated with the same DB type.

of $\Delta\bar{g}$ (353 to 453 ppm), belonging to the C2-type DBs. Visually, the remaining part appears as a cohesive whole, and a detailed analysis reveals that the *g*-shift values of C3-type DBs (520 to 568 ppm) and C1-type DBs (535 to 607 ppm) somewhat overlap. In order to get a clearer picture, GOAT optimization was carried out again, since each GOAT run for such a complex system as $C_{35}(NH_2)_{36}$ tends to converge to slightly distinct lowest-energy structures of DBs. The obtained conformers were combined with those from the previous GOAT run, and the Boltzmann-weighting procedure, along with *g*-tensor calculations, was repeated for the 30 lowest-energy samples out of the new combinations. The results (green triangles) from this double GOAT optimization, hereafter referred as double GOAT results, show that for C2-type DBs the variation range of $\Delta\bar{g}$ gets significantly reduced from 100 to 47 ppm. On the other hand, no evident gap is still observed between the *g*-shifts of C3-type and C1-type DBs. However, their values do not overlap anymore, falling in separate ranges from 531 to 567 ppm for the former and from 573 to 610 ppm for the latter. This also means that the variation range of $\Delta\bar{g}$ decreases from 48 to 36 ppm for C3-type DBs and from 72 to 37 ppm for C1-type DBs. Although these numbers are worse than the variation ranges observed for $C_{35}(OH)_{36}$, they are nevertheless below a solid threshold of 50 ppm, indicating that the geometrically equivalent DBs in $C_{35}(NH_2)_{36}$ can be grouped into three types as well. Another similarity with hydroxylated ND is that the lowest-energy DBs (black symbols) were identified as C1-type or irregular (i.e. formed of the NH_2-bonded dangling C atom) by both geometry optimization methods.

Concerning the energetics of DBs in $C_{35}(OH)_{36}$ and $C_{35}(NH_2)_{36}$, Figs. 4 and 5 demonstrate the distribution of isotropic *g*-shifts as a function of relative DB energies. Here, a zero value of ΔE represents the lowest-energy DBs, while others correspond to the higher-energy structures. In Fig. 4, the GOAT data of $C_{35}(OH)_{36}$ indicate that the span of ΔE values for all three DB types does not exceed 1 kcal/mol, but despite that, ΔE overlap between C1-type (0 to 0.5 kcal/mol) and C3-type (0.3 to 0.9 kcal/mol) DBs exists, making identification of DBs based solely on their energies from a single GOAT run rather complicated. In contrast, the double GOAT data of $C_{35}(NH_2)_{36}$ in Fig. 5 reveals that ΔE values for C1-type (0 to 4.9 kcal/mol), C2-type (20.1 to 23.2 kcal/mol)

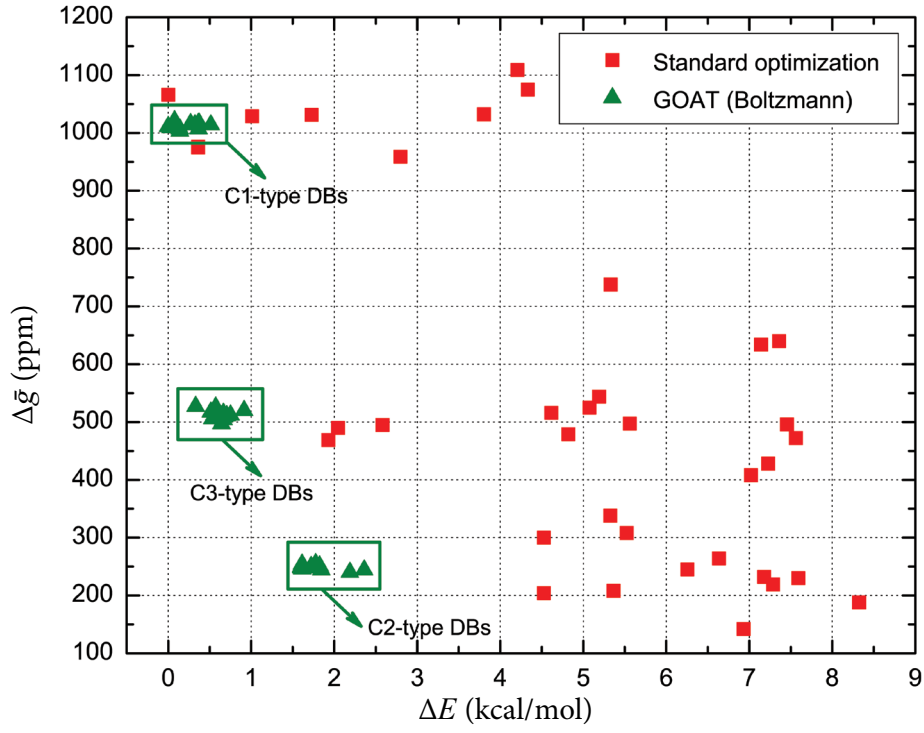

Fig. 4. Distribution of isotropic g-shifts $\Delta\bar{g}$ as a function of relative DB energies ΔE in $C_{35}(OH)_{36}$. A zero value of ΔE corresponds to the lowest-energy DBs. For clarity, green boxes indicate GOAT (Boltzmann) data points associated with the same DB type.

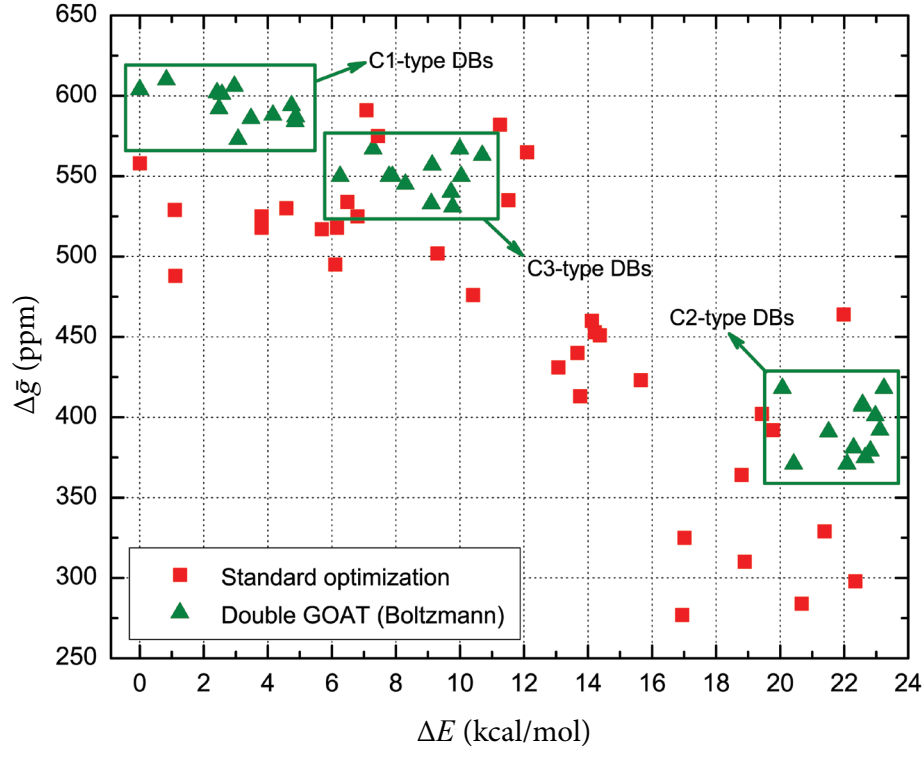

Fig. 5. Distribution of isotropic g-shifts $\Delta\bar{g}$ as a function of relative DB energies ΔE in $C_{35}(NH_2)_{36}$. A zero value of ΔE corresponds to the lowest-energy DBs. For clarity, green boxes indicate double GOAT (Boltzmann) data points associated with the same DB type.

and C3-type (6.3 to 10.7 kcal/mol) DBs do not overlap, although their spans are wider, varying from 3.1 to 4.9 kcal/mol. Needless to say, the presence of three distinct energy regions in $C_{35}(NH_2)_{36}$ supports the conclusion about three unique DB types derived from the previous analysis of $\Delta\bar{g}$ values. It should also be mentioned that for both NDs standard optimization yields highly scattered data, hindering a clear interpretation of DB behaviour.

The preceding analyses address the results for individual NDs, whereas experimentally one measures an average of $\Delta\bar{g}$ for the entire ensemble of nanoparticles in a sample. In order to account for the difference, we first introduce a simplifying assumption that the ND ensembles consist of diamond nanoparticles with identical shapes and sizes. This is not unreasonable, since centrifugation may separate nanoparticles not only by size but, possibly, by shape as well [35]. Considering that fabrication of NDs often involves processes such as crushing, grinding, or nanomilling [7], it is also reasonable to assume that the formation of their DBs occurs in a random manner. That being said, we averaged the isotropic *g*-shift values over all DBs introduced into a particular ND. In the case of $C_{35}(OH)_{36}$, the arithmetic average of $\Delta\bar{g}$ for the standard geometry optimization is 554 ppm, while the average for the GOAT optimization with the Boltzmann distribution is 591 ppm. It is interesting to note that the difference between these numbers is only 37 ppm, despite the highly distinct $\Delta\bar{g}$ distribution manner of individual DBs. For $C_{35}(NH_2)_{36}$, the corresponding numbers for the standard geometry optimization and the double GOAT optimization are 462 and 512 ppm, respectively, pointing to a very similar tendency observed for hydroxylated ND. From a statistical perspective, it seems that the standard geometry optimization yields fairly reliable data. However, in order to strengthen this assertion, we analyzed an additional system – a tetrahedrally shaped ND with a hydroxylated surface, $C_{51}(OH)_{52}$. Based on the knowledge gained from the investigation of $C_{35}(OH)_{36}$ in the current study, we focused on GOAT optimization for only four DBs that are known to be unique in analogous hydrogenated ND [30, 32; see Fig. 1(c)]. Once again, the Boltzmann distribution at a temperature of 300 K was applied for the 30 lowest-energy conformers of each DB. The average value of the resulting *g*-shifts was calculated by taking into account an appropriate contribution of each DB type to the total set of 52 DBs. Compared to the average of $\Delta\bar{g}$ for the standard geometry optimization of all 52 DBs (922 ppm) [9], the obtained GOAT average (866 ppm) is slightly lower, but the difference of 56 ppm is small enough to confirm our claim regarding the statistical reliability of the standard optimization data.

Summing up, the surface complexity of hydroxylated and aminated NDs makes it difficult for the standard geometry optimization procedure to converge to the lowest-energy configurations of DBs, whereas the application of GOAT enables one to identify the energetically lowest structures. The observation that the averaged isotropic *g*-shifts from the standard and GOAT optimizations coincide well for the investigated $C_{35}(OH)_{36}$, $C_{35}(NH_2)_{36}$ and $C_{51}(OH)_{52}$ nanoparticles suggests that our previously obtained statistical data for hydroxylated and aminated NDs of other shapes and sizes [9] are also valid, despite the improperly captured individual behaviour of DBs. In addition, herein we provide a strong evidence that hydroxylated and aminated NDs do possess geometrically equivalent DBs, thereby dispelling our earlier doubts about their existence [9, 32]. This is very important for future studies on similar NDs with fully functionalized surfaces because, in order to obtain a complete picture of this type of magnetic behaviour or other properties, it is no longer necessary to consider all possible DBs in the system, allowing a reliable analysis with much less effort.

4. Conclusions

To conclude, the GOAT algorithm was used to search for the lowest-energy structures of DBs introduced into hydroxylated and aminated NDs. By comparing the isotropic *g*-shifts of the obtained conformers, it is revealed that only three unique DBs out of 36 available ones exist in octahedrally shaped $C_{35}(OH)_{36}$ and $C_{35}(NH_2)_{36}$, consistent with the nature of analogous but structurally less complex systems like $C_{35}H_{36}$ or $C_{35}F_{36}$. This finding facilitates future studies on similar NDs with fully functionalized surfaces by allowing the investigation of their DBs at a significantly reduced computational cost. The *g*-tensor calculations based on the geometries

from the standard optimization indicate that the behaviour of individual DBs is not properly captured using such an approach. However, the arithmetically averaged *g*-shifts, potentially reflecting experimental conditions, demonstrate a fairly good agreement with the GOAT results. This trend was also confirmed by an additional investigation on the hydroxylated ND of tetrahedral shape.

References

[1] N. Nunn, M. Torelli, G. McGuire, and O. Shenderova, Nanodiamond: A high impact nanomaterial, Curr. Opin. Solid State Mater. Sci. **21**, 1 (2017), https://doi.org/10.1016/j.cossms.2016.06.008

[2] S. Chauhan, N. Jain, and U. Nagaich, Nanodiamonds with powerful ability for drug delivery and biomedical applications: Recent updates on in vivo study and patents, J. Pharm. Anal. **10**, 1 (2020), https://doi.org/10.1016/j.jpha.2019.09.003

[3] C. Fryer, P. Murray, and H. Zhang, Modification of nanodiamonds for fluorescence bioimaging, RSC Adv. **14**, 4633 (2024), https://doi.org/10.1039/D3RA08762J

[4] N. Priyadarshni, R. Singh, and M.K. Mishra, Nanodiamonds: Next generation nano-theranostics for cancer therapy, Cancer Lett. **587**, 216710 (2024), https://doi.org/10.1016/j.canlet.2024.216710

[5] D.E.J. Waddington, M. Sarracanie, H. Zhang, N. Salameh, D.R. Glenn, E. Rej, T. Gaebel, T. Boele, R.L. Walsworth, D.J. Reilly, and M.S. Rosen, Nanodiamond-enhanced MRI via *in situ* hyperpolarization, Nat. Commun. **8**, 15118 (2017), https://doi.org/10.1038/ncomms15118

[6] D.E.J. Waddington, T. Boele, E. Rej, D.R. McCamey, N.J.C. King, T. Gaebel, and D.J. Reilly, Phase-encoded hyperpolarized nanodiamond for magnetic resonance imaging, Sci. Rep. **9**, 5950 (2019), https://doi.org/10.1038/s41598-019-42373-w

[7] A.I. Shames and A.M. Panich, Chapter 6 – Paramagnetic defects in nanodiamonds, in: *Nanodiamonds: Advanced Material Analysis, Properties and Applications*, ed. J.C. Arnault (Elsevier, Amsterdam, 2017) pp. 131–154, https://doi.org/10.1016/B978-0-32-343029-6.00006-4

[8] M. Barzegar Amiri Olia, P.S. Donnelly, L.C.L. Hollenberg, P. Mulvaney, and D.A. Simpson, Advances in the surface functionalization of nanodiamonds for biological applications: A review, ACS Appl. Nano Mater. **4**, 9985 (2021), https://doi.org/10.1021/acsanm.1c02698

[9] Š. Masys, V. Jonauskas, and Z. Rinkevicius, Electronic *g*-tensors of dangling bonds in hydroxylated and aminated nanodiamonds: A computational study, Phys. Scr. **100**, 015402 (2024), https://doi.org/10.1088/1402-4896/ad9555

[10] V. Barone and P. Cimino, Validation of the B3LYP/N07D and PBE0/N07D computational models for the calculation of electronic *g*-tensors, J. Chem. Theory Comput. **5**, 192 (2009), https://doi.org/10.1021/ct800279g

[11] A.M. Panich, N.A. Sergeev, and S.D. Goren, Location of paramagnetic defects in detonation nanodiamond from proton spin-lattice relaxation data, Solid State Nucl. Magn. Reson. **105**, 101624 (2020), https://doi.org/10.1016/j.ssnmr.2019.101624

[12] F. Neese, Software update: The ORCA program system–version 6.0, WIREs Comput. Mol. Sci. **15**, e70019 (2025), https://doi.org/10.1002/wcms.70019

[13] B. de Souza, GOAT: A global optimization algorithm for molecules and atomic clusters, Angew. Chem. Int. Ed. **64**, e202500393 (2025), https://doi.org/10.1002/anie.202500393

[14] C. Bannwarth, S. Ehlert, and S. Grimme, GFN2-xTB – An accurate and broadly parametrized self-consistent tight-binding quantum chemical method with multipole electrostatics and density-dependent dispersion contributions, J. Chem. Theory Comput. **15**, 1652 (2019), https://doi.org/10.1021/acs.jctc.8b01176

[15] C. Bannwarth, E. Caldeweyher, S. Ehlert, A. Hansen, P. Pracht, J. Seibert, S. Spicher, and S. Grimme, Extended tight-binding quantum chemistry methods, WIREs Comput. Mol. Sci. **11**, e1493 (2021), https://doi.org/10.1002/wcms.1493

[16] F. Neese, The ORCA program system, WIREs Comput. Mol. Sci. **2**, 73 (2012), https://doi.org/10.1002/wcms.81

[17] F. Neese, F. Wennmohs, U. Becker, and C. Riplinger, The ORCA quantum chemistry program package, J. Chem. Phys. **152**, 224108 (2020), https://doi.org/10.1063/5.0004608

[18] S. Ehlert, M. Stahn, S. Spicher, and S. Grimme, Robust and efficient implicit solvation model for fast semiempirical methods, J. Chem. Theory Comput. **17**, 4250 (2021), https://doi.org/10.1021/acs.jctc.1c00471

[19] Š. Masys, Z. Rinkevicius, and J. Tamulienė, On the magnetic properties of nanodiamonds: Electronic *g*-tensor calculations, J. Chem. Phys. **151**, 044305 (2019), https://doi.org/10.1063/1.5111024

[20] A.D. Becke, Density-functional thermochemistry. III. The role of exact exchange, J. Chem. Phys. **98**, 5648 (1993), https://doi.org/10.1063/1.464913

[21] P.J. Stephens, F.J. Devlin, C.F. Chabalowski, and M.J. Frisch, *Ab initio* calculation of vibrational absorption and circular dichroism spectra using density functional force fields, J. Phys. Chem. **98**, 11623 (1994), https://doi.org/10.1021/j100096a001

[22] R. Krishnan, J.S. Binkley, R. Seeger, and J.A. Pople, Self-consistent molecular orbital methods. XX. A basis set for correlated wave functions, J. Chem. Phys. **72**, 650 (1980), https://doi.org/10.1063/1.438955

[23] M.J. Frisch, J.A. Pople, and J.S. Binkley, Self-consistent molecular orbital methods 25. Supplementary functions for Gaussian basis sets, J. Chem. Phys. **80**, 3265 (1984), https://doi.org/10.1063/1.447079

[24] S. Koseki, M.W. Schmidt, and M.S. Gordon, MCSCF/6-31G(d,p) calculations of one-electron spin–orbit coupling constants in diatomic molecules, J. Phys. Chem. **96**, 10768 (1992), https://doi.org/10.1021/j100205a033

[25] S. Koseki, M.S. Gordon, M.W. Schmidt, and N. Matsunaga, Main group effective nuclear charges for spin–orbit calculations, J. Phys. Chem. **99**, 12764 (1995), https://doi.org/10.1021/j100034a013

[26] S. Koseki, M.W. Schmidt, and M.S. Gordon, Effective nuclear charges for the first- through third-row transition metal elements in spin–orbit calculations, J. Phys. Chem. A **102**, 10430 (1998), https://doi.org/10.1021/jp983453n

[27] F. Neese, An improvement of the resolution of the identity approximation for the formation of the Coulomb matrix, J. Comput. Chem. **24**, 1740 (2003), https://doi.org/10.1002/jcc.10318

[28] F. Neese, F. Wennmohs, A. Hansen, and U. Becker, Eflcient, approximate and parallel Hartree–Fock and hybrid DFT calculations. A 'chain-of-spheres' algorithm for the Hartree–Fock exchange, Chem. Phys. **356**, 98 (2009), https://doi.org/10.1016/j.chemphys.2008.10.036

[29] F. Weigend, Accurate Coulomb-fitting basis sets for H to Rn, Phys. Chem. Chem. Phys. **28**, 1057 (2006), https://doi.org/10.1039/B515623H

[30] Š. Masys, Z. Rinkevicius, and J. Tamulienė, Electronic *g*-tensors of nanodiamonds: Dependence on the size, shape, and surface functionalization, J. Chem. Phys. **151**, 144305 (2019), https://doi.org/10.1063/1.5121849

[31] Š. Masys, Z. Rinkevicius, and J. Tamulienė, Computational study on the electronic *g*-tensors of hydrophilic and hydrophobic nanodiamonds interacting with water, J. Chem. Phys. **152**, 144302 (2020), https://doi.org/10.1063/5.0001485

[32] Š. Masys, V. Jonauskas, and Z. Rinkevicius, Electronic *g*-tensor calculations for dangling bonds in nanodiamonds, J. Phys. Chem. A **125**, 8249 (2021), https://doi.org/10.1021/acs.jpca.1c06253

[33] Š. Masys, V. Jonauskas, and Z. Rinkevicius, Geometries of defects in nanodiamonds optimized with the low-cost methods: How good are they for the electronic g-tensor calculations?, Diam. Relat. Mater. **136**, 110009 (2023), https://doi.org/10.1016/j.diamond.2023.110009

[34] K. Momma and F. Izumi, VESTA3 for three-dimensional visualization of crystal, volumetric and morphology data, J. Appl. Crystallogr. **44**, 1272 (2011), https://doi.org/10.1107/S0021889811038970

[35] S. Eldemrdash, G. Thalassinos, A. Alzahrani, Q. Sun, E. Walsh, E. Grant, H. Abe, T.L. Greaves,

T. Ohshima, P. Cigler, P. Matjíek, D.A. Simpson, A.D. Greentree, G. Bryant, B.C. Gibson, and P. Reineck, Fluorescent HPHT nanodiamonds have disk- and rod-like shapes, Carbon **206**, 268 (2023), https://doi.org/10.1016/j.carbon.2023.02.018

NEKOMPENSUOTIEJI RYŠIAI HIDROKSILO IR AMINO GRUPĖMIS FUNKCIONALIZUOTUOSE NANODEIMANTUOSE: GLOBALIOSIOS OPTIMIZACIJOS ALGORITMO TAIKYMAS

Š. Masys, V. Jonauskas [a], Ž. Rinkevičius [b]

[a] *Vilniaus universiteto Fizikos fakulteto Teorinės fizikos ir astronomijos institutas, Vilnius, Lietuva*

[b] *Karališkojo technologijos instituto Chemijos, biotechnologijos ir sveikatos inžinerijos mokslų mokyklos Teorinės chemijos ir biologijos departamentas, Stokholmas, Švedija*

Santrauka

Nanodeimantai (ND) yra deimanto nanodalelės, kurių dydis siekia nuo apytiksliai vieno iki keliolikos dešimčių nanometrų. Jos pasižymi nanomedicinai itin tinkamomis savybėmis: išskirtiniu biosuderinamumu, didele pernašos talpa bei nepaprastai gausia paviršiaus funkcinių grupių įvairove. Tačiau vienas iš ND panaudojimo trūkumų – sudėtinga sekti jų lokalizaciją ir judėjimą *in vivo*, todėl tai apriboja galimybę stebėti ilgalaikio gydymo eigą. Vis dėlto tiek magnetinio rezonanso, tiek fluorescencijos pagrindo ND vizualizacija yra įmanoma, bet tam būtini paramagnetiniai defektai. Kadangi nekompensuotieji ryšiai (NR) yra vieni iš dažniausiai ND susidarančių paramagnetinių defektų, šiame darbe tiriama jų geometrinė konfigūracija hidroksilo ir amino grupėmis funkcionalizuotuose ND. Atsižvelgus į tokių ND paviršiaus geometrinį sudėtingumą, tyrimams taikytas globaliosios optimizacijos algoritmas, kuris, priešingai nei standartinė geometrijos optimizacijos procedūra, užtikrina visuotinai žemiausios sistemos būsenos paiešką. Optimizuotos NR struktūros buvo panaudotos įvertinant elektroninį *g*-tenzorių – vieną svarbiausių elektronų paramagnetinio rezonanso parametrų. Gauti rezultatai rodo, kad oktaedrinės formos $C_{35}(OH)_{36}$ ir $C_{35}(NH_2)_{36}$ nanodalelėse egzistuota tik trys unikalūs NR, o tai suteikia vertingos informacijos ateities ND tyrimams ir leidžia reikšmingai sutaupyti skaičiavimo laiko ir išteklių.